JOURNAL OF APPLIED PHYSICS **98**, 084904 (2005)

Metal-organic chemical-vapor deposition of $(Ba,Sr)TiO_3$: Nucleation and growth on Pt-(111)

S. Regnery, Y. Ding, P. Ehrhart,[a] C. L. Jia, K. Szot, R. Thomas, and R. Waser
Institut für Festkörperforschung (IFF) and Center of Nanoelectronic Systems for Information Technology (CNI), Forschungszentrum Jülich, D-52425 Jülich, Germany

(Received 22 February 2005; accepted 30 August 2005; published online 21 October 2005)

Thin films of the $(Ba_xSr_{1-x})TiO_3$ (BST) solid solution series were grown by metal-organic chemical-vapor deposition (MOCVD) on platinized silicon wafers with emphasis to $(Ba_{0.7}Sr_{0.3})TiO_3$ and $SrTiO_3$. The nucleation behavior and the size of the stable nuclei were investigated by different scanning probe microscope techniques including local conductivity scanning. The characteristic differences were observed for different deposition temperatures, i.e., a homogeneous nucleation of small BST grains on the larger Pt grains at 565 °C and a dominating grain-boundary nucleation at 655 °C. X-ray photoelectron spectroscopy indicates a stoichiometric composition from the beginning. The microstructural evolution was investigated by high-resolution transmission electron microscopy and revealed randomly oriented grains (typical in-plane size 10–20 nm) with a high density of twins at 565 °C and (100)-oriented defect-free grains of slightly increased size at 655 °C. This remarkably stable (100) texture seems specific for MOCVD as it is not observed for other deposition methods. The grain structure and surface morphology and their dependence on film stoichiometry (group-II/Ti ratio) are investigated. The relation between the structural and the electrical properties, capacitance, and leakage current, is finally discussed. © *2005 American Institute of Physics*. [DOI: 10.1063/1.2084312]

I. INTRODUCTION

Perovskite oxide thin films with a high dielectric constant (high *K*), such as $(Ba_xSr_{1-x})TiO_3$ (BST), have been proposed for a very broad application area, including capacitor dielectrics for future dynamic random access memories (DRAMs), embedded capacitors, tunable devices, as well as gate oxides for field-effect transistors.[1] For capacitor applications of BST films, i.e., metal-insulator-metal (MIM) structures, Pt is considered as a standard metal electrode[2,3] due to its stability against oxidation at the deposition temperatures and its rather low leakage currents, which might be related to its high work function. Especially the lower leakage currents compared to Ir/IrO_2 (Ref. 3) or Ru/RuO_2 (Ref. 4–6) electrodes seem to overwhelm the disadvantages of a more difficult etching process.[3]

In spite of intensive research over the last two decades[2,7] many details of the nucleation and growth of BST films and on the structure-property relations are not understood in detail. With MOCVD (metal-organic chemical-vapor deposition) different textures of the films have been observed for different deposition temperatures, e.g., typically BST-(100) on Pt-(111) for temperatures above 600 °C and more randomly orientated grains at lower temperatures.[8–10] However, details of the nucleation and growth behavior are still unknown and there is especially a difference to sputter deposition[11] or laser ablation[12] where more (110)-or (111)-oriented films are observed at deposition temperatures above 600 °C and to chemical solution deposition (CSD) where nearly epitaxial growth of $SrTiO_3$ (STO) may be obtained on Pt-(111).[13] In addition the possible influence of the process conditions during nucleation might be important as shown for the deposition of $Pb(Zr,Ti)O_3$.[14] In this study a broad spectrum of analytic methods was used to get a more detailed understanding on nucleation and growth. In addition we discuss the influence of the microstructure on the electrical properties.

II. EXPERIMENTAL DETAILS

A. MOCVD reactor

BST films were deposited in an AIXTRON 2600G3 Planetary Reactor®, which can handle five 6-inch wafers simultaneously, and which has been described previously.[15] The main process conditions are summarized in Table I. The temperature of the wafer surface can be assumed to be 20–50 °C lower than the directly measured susceptor temperature. The liquid precursors $Sr(thd)_2$, $Ba(thd)_2$, and $Ti(O\text{–}i\text{Pr})_2(thd)_2$ were dissolved in butyl acetate and injected by an ATMI-300B or an AIXTRON TRIJET® liquid delivery system. Due to four independent sources the TRIJET has a higher flexibility allowing for the deposition of different nucleation layers and multilayers. For the ATMI system a 0.35*M* solution was used, whereas a higher dilution of the precursors, 0.05*M*, was necessary for the TRIJET. This higher amount of injected solvent presents no major problem with the present precursors diluted in butylacetate.[16] Due to the pulsed injection (droplet size ~5 μl; frequency ~1 Hz) the average oxidizer flow rate was increased for the TRIJET system.

B. Film composition and thickness

Routinely, x-ray fluorescence spectroscopy (XRF) was used for the determination of composition and the areal mass density of the films.[17] CSD-deposited films of similar com-

---

[a] Electronic mail: p.ehrhart@fz-juelich.de

TABLE I. MOCVD process parameters.

Vaporizer	LDS-300B	TRIJET
Average precursor flow	0.08 ml/min	0.9 ml/min
Precursor concentration[a]	0.35M	0.05M
Vaporizer temperature	~240 °C	~240 °C
Reactor		
Oxygen flow rate	55 SCCM[b]	70 SCCM
N_2O flow rate	55 SCCM	70 SCCM
Total Ar carrier flow	2400 SCCM	1440 SCCM
Susceptor temperature	565 °C, 655 °C	
Process pressure	2.0 mbars	
Growth rate	2–4 nm/min	
Nominal film thickness	0.3-100 nm	
Film stoichiometry: Ba/Sr; group-II/Ti	$(Ba_{0.7}Sr_{0.3})TiO_3$–$SrTiO_3$; 0.9–1.1	

[a] Initial concentration of the individual precursors before mixing.

[b] SCCM denotes cubic centimeter per minute at standard temperature and pressure.

position were used as calibration standards. Generally, we used $Pt/TiO_2/SiO_x/Si$ substrates with a platinum thickness of 100 nm. In order to avoid interference with the adhesion layer, substrates with ZrO_2 instead of TiO_2 adhesion layers were used additionally. The film thickness was deduced from the areal mass density using the bulk densities of BST and STO. These values yield a lower limit for the actual thickness but were confirmed for some films by the thickness fringes observed by x-ray diffraction[10] (XRD). Because precise measurements are limited to thickness of about >5 nm, the nominal thickness of thin-film samples (0.3, 0.5, and 1.5 nm) was calculated from the deposition time; due to an uncertainty of about 3 s in the switching time of the run-vent valve we have to consider an error of 30% in thickness for these thinnest films. The composition of the nucleation layers was determined by x-ray photoelectron spectroscopy (XPS) using a Physical Electronics 1600-XPS instrument. We used monochromatic Al K_α radiation for the excitation and a pass energy of 24 or 11.7 eV for the analyzer.

C. Structural characterization

Standard XRD characterization was performed with a Philips Xpert MRD system using Cu K_α radiation and a diffracted beam monochromator. Scanning probe microscopy (SPM) was performed with a JEOL 4210 system. A contact mode was used for mapping the electrical conductivity. For the conductivity scans 0.1 V was applied between the cantilever tip (PtIr, $r_0 \sim 20$ nm) and the clean or partly covered platinum bottom electrode. Assuming that high-resistivity areas can be related to the deposited BST, this mapping gives a good location of initial nuclei in relation to the larger platinum grains. Scanning force microscopy (SFM) images of the surface morphology of the BST films could be simultaneously obtained in the contact mode. However, much better resolution was obtained for separately optimized scans in the ac-SFM mode. Transmission electron microscopy (TEM) and high-resolution transmission electron microscopy (HRTEM) investigations were carried out using a JEOL 4000EX electron microscope with a Scherzer resolution of 0.17 nm at 400 kV. Cross-sectional as well as backside-polished plane-view samples were prepared from the original wafers. After mechanical grinding and dimpling, these specimens were ion milled to perforation on a stage cooled by liquid nitrogen.

D. Electrical characterization

For electrical measurements, Pt electrode pads were sputter deposited on top of the BST films and patterned using shadow masks or liftoff lithography. An additional post annealing was performed at 550 °C for the Pt/BST/Pt MIM structures in order to anneal the damage induced by the sputtering. As this annealing is performed at a lower temperature than the depositions, the electrical characterization relates to the as-deposited films. The capacitance-voltage curves were obtained with a HP #4284 LCR meter using a frequency of 100 kHz. The leakage currents were measured using a Burster 4462 voltage generator and a Keithley 617 electrometer with a detection limit of 50 fA.

III. NUCLEATION ON PT-(111)

A. Surface morphology of the Pt substrate

The surface morphology of the platinized substrate, $Pt(100\ nm)/TiO_2(10\ nm)/SiO_2(400\ nm)/Si$, is decisive for the control of the nucleation. Figure 1 shows SFM images of the Pt surface: (a) the as-deposited state after sputter deposition at ~150 °C, (b) annealed in artificial air at 600 °C, and (c) at 700 °C. We observe a minor grain growth after annealing up to 600 °C and an appreciable grain growth at 700 °C. Part (d) shows an in-plane TEM micrograph, which confirms that the SPM contrast can essentially be attributed to the grain structure and establishes the in-plane grain size of 50–150 nm for the Pt layer. In addition, the perfection of the (111) texture of the Pt is increased by the annealing and is nearly perfect already at 600 °C. The roughness of the surface, as quantified by the root-mean-square (rms) variation, was ~1.5 nm and decreased slightly with annealing. An investigation of the evolution of the roughness of the stack, SiO_2–TiO_2–Pt, revealed that an appreciable increase of the surface roughness is observed after the deposition of the TiO_2 adhesion layer and this roughness therefore seems to

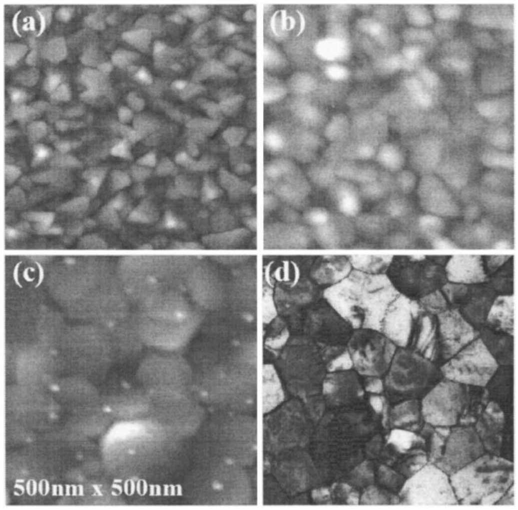

FIG. 1. SPM images of 0.5×0.5 μm^2 areas of the surface of the Pt electrode: (a) as-deposited, (b) annealed at 600 °C, and (c) annealed at 700 °C. For improved resolution of the very small grains part (a) was imaged in the scanning tunneling mode whereas part (b) and (c) are imaged in the SFM mode similar to the insulating layers discussed below. The furnace annealing was performed at the indicated temperatures for 30 min in artificial air. Part (d) shows a TEM micrograph of the grain structure after the standard annealing at 600 °C.

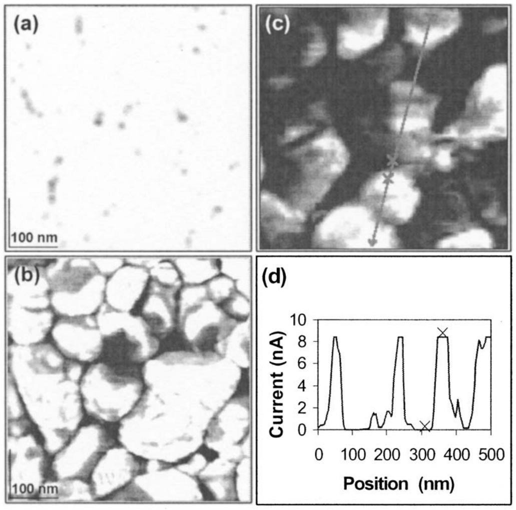

FIG. 2. SFM conductivity mapping with images sizes of 0.5×0.5 μm film areas: (a) bare Pt substrate and (b) 0.3-nm BST layer grown at 655 °C. Low conductivity is observed at the platinum grain boundaries. (c) 0.5-nm BST layer; only small regions with maximum conductivity are left. The current along the line indicated in the figure is plotted in part (d).

control also the final roughness of the Pt layer. Due to the different thermal-expansion coefficients of the Si substrate and the Pt, the Pt layer is under thermally induced tensile stress after annealing. XRD yields a tetragonal distortion of ~0.5% corresponding to c/a ratio of 0.995. This value corresponds to a tensile stress of 550 MPa, and is in agreement with measurements of the wafer bending.[18] As the actual surface temperatures during deposition were not higher than 600 °C we used a standard preanneal, i.e., 30 min at 600 °C, to stabilize the microstructure before deposition. The stability of this surface morphology was verified after removing the BST layer for some test films.

It might be worth to note that the resolution of the SFM is limited due to the immediate formation of an adsorbent layer at Pt surfaces under atmospheric conditions. Even under vacuum conditions such adsorbents are present at room temperature, as shown by the $C1s$ and $O1s$ lines in the XPS spectra, and an *in situ* surface cleaning is necessary. However, this clean surface does not represent the actual surface conditions during MOCVD at 600 °C.

B. Structural features of the nuclei

The deposition of the BST is most sensitively monitored by conductivity mapping images. Figure 2(a) shows the platinum substrate. The image is dominated by the homogeneous distribution of the maximum conductivity, i.e., a current of almost 10 nA, which is limited by the actual contact surface between tip and bottom electrodes. Randomly orientated darker spots indicate simply disruption during mapping or the mapping of grain boundaries as suggested by the good correlation of the structures with the TEM micrograph of the gain structure, Fig. 1(b).

Figure 2(b) shows a very thin film, nominally 0.3 nm, grown at 655 °C, where we do not expect a complete coverage. Indeed, the deposited material first accumulates in the region of the platinum grain boundaries. Hence, the platinum grain structure is now clearly visible. This is an indication that the diffusion length of the adatoms at 655 °C is larger than the grain size of the platinum of ~100 nm. For an increased thickness of 0.5 nm, Fig. 2(c), the insulating area has increased and most of the surface is covered. Nevertheless, some areas with the maximum conductivity of 10 nA, which indicates uncovered Pt, are left as indicated in the line scan shown in Fig. 2(d). In addition to the preferred nucleation at grain boundaries there are some nucleation in between, which finally yields much smaller grain sizes for BST than for the underlying Pt. The nature of these additional nucleation sites (e.g., surface steps and kinks) could not be identified in SFM images, even when they were recorded separately under optimized conditions. The rms roughness of 0.9–1.5 nm was somewhat lower than that for the initial Pt substrates of ~1.5 nm, and this difference may be indicative for the preferred nucleation at grain boundaries and the connected flattening of the grooves.

The conductivity scan for a 0.5-nm STO film, which was deposited at 655 °C, is shown in Fig. 3(a) and is very similar to the scans for BST. The deposition starts again along the grain boundaries of the platinum grains. Figure 3(b) shows

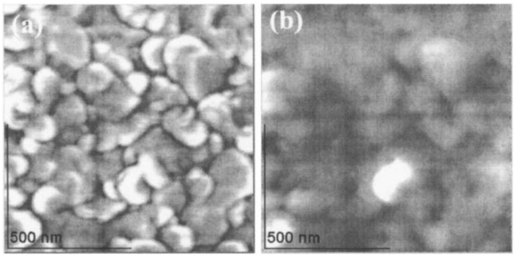

FIG. 3. Simultaneously recorded conductivity (a) and topography (b) for a nominally 0.5-nm-thick STO film deposited at 655 °C. The surface area is 0.5×0.5 μm.

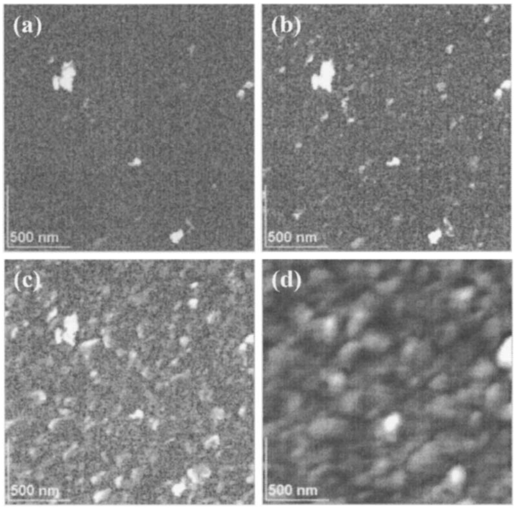

FIG. 4. Dependence of the surface conductivity on the bias voltage applied at the SPM tip. The scanned area is $2 \times 2\ \mu m^2$. (a) bias voltage =0.5 V, (b) bias =1.3 V, and (c) bias =2.0 V; (d) topographical image taken simultaneously in the contact mode which is similar for all scans.

the topography as recorded simultaneously in contact mode. In spite of the limited resolution the higher areas can be related to the areas with higher conductivity, which corresponds to lower coverage. After a nominal thickness of 1.5 nm the films can be considered closed as no high conductivity could be detected except for some spots, which were used as a marker, Fig. 4(a). Nevertheless, by increasing the bias voltage tunneling currents increase and the grain structure gets visible again, as demonstrated in Figs. 4(b) and 4(c).

Details of a nominally 1.5-nm thick BST film deposited again at 655 °C, are shown in Fig. 5 in a cross-sectional HRTEM micrograph. The film is essentially closed, and there is a good consistency with the calculated thickness of 1.5 nm. The arrows indicate areas where the crystallized BST can be seen. However, at some different spots the platinum patterning goes through the whole film, which implies that there are actually areas with less deposition but they are very rare.

Figure 6 shows conductivity scans for a nominally 0.3-nm thick film deposited at 565 °C. The brightest parts have a similar conductivity as observed after deposition at 655 °C, but the main area of the platinum grains is covered with insulating BST and there is no longer a preferred nucleation at the Pt grain boundaries. In addition, there is some indication for an ordering of the low conductivity areas on a typical length scale of about 30 nm. A sample with 0.5 nm thickness shows no significant difference in these structures and Fig. 7(a) shows a high-resolution SFM image, which was recorded independently in the ac-SFM mode. We observe round nuclei with a size between 10 and 20 nm and there is an indication for an agglomeration without coalescence and structural rearrangement. Nevertheless, these agglomerates might explain the structure observed in the conductivity scans. For a further growth stage, 3.0 nm thickness [Fig. 7(b)], we can assume that the layer is now completely closed and the dominant structures must be considered as replicas of the platinum structure. Additionally, we observe again some line structure on the platinum grains, which is in good correlation with the structures on a length scale of ~30 nm observed in Fig. 6, however, the resolution is not sufficient for further atomic details.

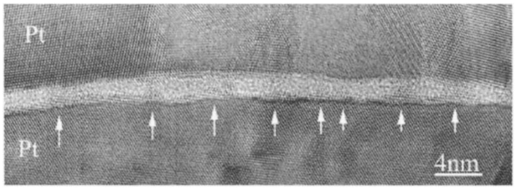

FIG. 5. HRTEM of a cross section of a nominally 1.5-nm-thick BST film. The film has been covered with an additional Pt layer for the preparation of the cross section. The arrows indicate regions were crystalline BST is identified.

C. Chemistry of the nuclei

The chemistry of the nuclei was investigated by XPS, and the intensities of the observed platinum, titanium, barium, and strontium lines are summarized in Fig. 8 for deposition temperatures of 655 and 565 °C, respectively. The XPS line intensities of Ba, Sr, and Ti are normalized to the intensities of a 86-nm thick film, which was also analyzed by XRF and had a composition of Ti:Ba:Sr of 100:70:30. For the Pt we observe a small change of the binding energy between the free Pt surface and the covered Pt and a steady decrease of the Pt signal along with the increase of the Ti, Ba, and Sr line intensities. Although there are indications for a Ti enrichment of the film at ~1.5 nm thickness, the error bars at the lowest film thickness are too large for a quantitative determination of the elemental ratios, and possible influences of catalytic effects of the initial Pt surface[19] remain speculative. Angular resolved XPS was additionally performed and Fig. 9 shows the example of a 1.5 nm film de-

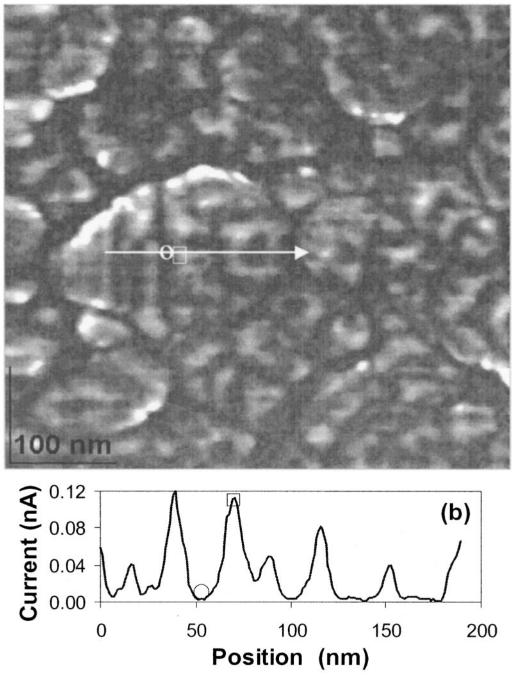

FIG. 6. Conductivity map of a 0.3-nm BST/Pt film deposited at 565 °C. Image size: $0.5 \times 0.5\ \mu m^2$. A line scan shows the modulation of the deposition on a platinum grain.

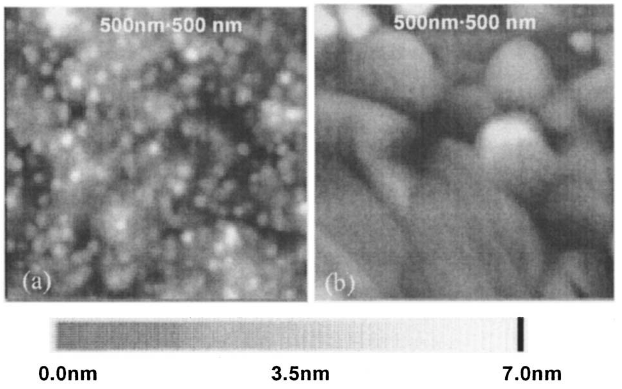

FIG. 7. SFM topography in ac mode of BST films grown at 565 °C. (a) 0.5 nm average thickness. The size of the nuclei can be estimated to 10-25 nm. (b) 3.0 nm thickness; the film can considered to be coalesced and the main features are induced from the Pt substrate.

posited at 655 °C. The relative change of the different line intensities is shown after the change of the takeoff angle from 45° to 5°. The Ti, Ba, and Sr signals increase in a similar way due to the less deep sampling volume, whereas the Pt signal is reduced. This behavior indicates a rather homogeneous film. Most importantly, independent of the larger error bars at very thin films we observe all elements, Ba, Sr, and Ti, beginning from the thinnest layer, i.e., there is nucleation of the mixed oxide from the very beginning.

IV. FILM GROWTH AND MICROSTRUCTURAL EVOLUTION

After the formation of a coalesced film the conductivity scanning is no longer applicable and we mainly rely on XRD and electron microscopy. We will first present some characteristic features at the example of Ti-rich films, which were deposited at 655 °C. Subsequently, we discuss the most relevant changes observed for lower deposition temperatures and for different film stoichiometries. Finally, changes with film thickness, which are important for the evaluation of electrical properties, will be discussed.

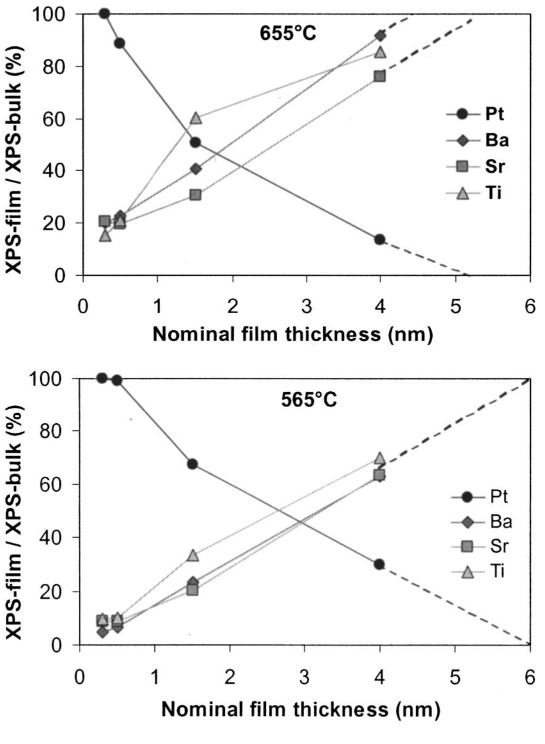

FIG. 8. Relative concentration of the elements as determined by XPS as a function of the film thickness for films deposited at 655 and 565 °C.

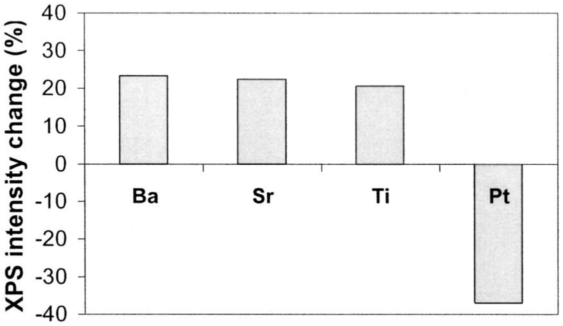

FIG. 9. Angular resolved XPS indicating no thickness dependence of the atomic ratios for a 1.5-nm-thick film.

A. Ti-rich films (group-II/Ti∼0.9–0.99) deposited at 655 °C

Films of typical thickness of 20–30 nm generally show a nearly perfect (100) texture on Pt-(111).[8–10,20] The mosaic width is 2°–3° similar to the underlying Pt.[15] After cooling down from the deposition temperature the BST is under thermal stress due to the different thermal-expansion coefficient from the Si substrate. Figure 10 shows an example of a residual stress measurement, which yields the expected straight line in a $\sin^2\psi$ plot. The extrapolated value of Δd at $\sin^2\psi = 1$ corresponds to the tetragonal distortion of the film which can be quantified by the distortion $\varepsilon=\Delta d/d$ or by the c/a ratio$=(d+\Delta d)/d$. The observed strain corresponds to tensile stress within the plane of this film, $\varepsilon=-0.95\%$ or $c/a=0.99$. For different films this strain varied between -0.6% and -1.1%, due to variations in the quality of the film and the Pt electrode. However, no systematic dependence on

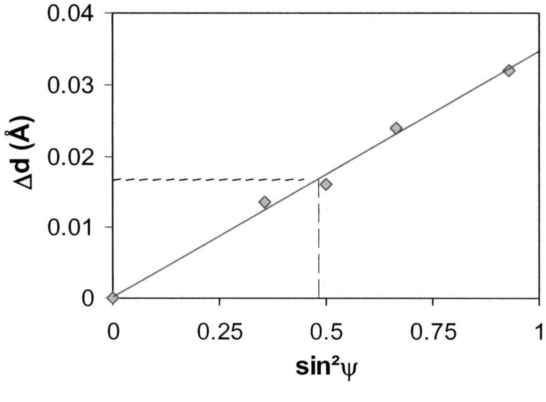

FIG. 10. Evaluation of the film strain in a $\sin^2\psi$ plot for sample grown at 625 °C. The arrows indicate the evaluation of the unstrained lattice parameter of the bulk. Due to the fiber structure data points correspond to special film orientations: $\psi=0°:(002)$, $\psi=36.7°:(123)$; $\psi=45.0°:(022)$, $\psi=54.7°:(111)$; $\psi=74.5°:(321)$.

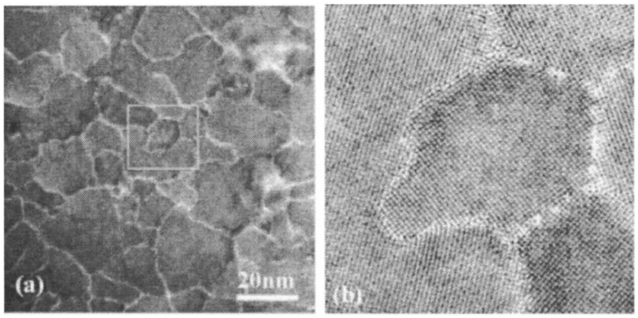

FIG. 11. In-plane HRTEM images of a 30-nm-thick Ti-rich BST film (group-II/Ti=0.95), which was deposited at 655 °C. Part (b) shows the grain indicated in part (a) in larger magnification. (a) Grain distribution and (b) lattice rows indicating <001> orientation and indications of the grain-boundary structure.

the deposition temperature was observed. From this measured strain ε the film stress σ can be estimated in an approximation of elastic isotropy,[21]

$$\sigma = \varepsilon\ E/(\nu+1), \tag{1}$$

where E= Young's modulus and ν= Poisson's ratio. From the average strain of $\varepsilon=(-0.85\pm0.25)\%$ we obtain a stress of $\sigma=800\pm200$ MPa using $E=135$ GPa and $\nu=0.32$.[22] This value is in reasonable agreement with direct stress measurements of ~610 MPa from the wafer bending.[22] Larger values for the stress, ~1200 MPa, might be obtained by using elastic constants derived from single-crystal data for $BaTiO_3$,[23] which are, however, still lower than earlier values of 2200 MPa as deduced from strain measurements.[24]

As indicated in Fig. 10, additionally, the lattice parameter of the unstrained bulk material can be deduced from the value of Δd at $\sin^2\psi=2v/(v+1)$, which is ~0.485 for the present case. The c/a ratio is always smaller than 1, i.e., opposite to the ferroelectric phase, which is characterized by a larger c axis. The substrate-induced opposite distortion yields therefore a plausible argument for the generally observed suppression of the phase transition in these films, which has been discussed in detail recently.[25]

We observe a quite stable columnar growth as evidenced by scanning electron microscopy (SEM) (Ref. 26 and Fig. 21 below). Additional details on the grain structure are revealed by in-plane HRTEM images from backside-polished films. Figure 11(a) shows a 30 nm thick, slightly Ti-rich film of BST deposited at 655 °C. The average grain size is about 10-30 nm. Figure 11(b) shows the magnification of the grain indicated in Fig. 11(a) and reveals a perfect crystal structure with (100) orientation as well as the disturbed structure at the grain boundary. Figure 12 shows a cross-sectional image of the Pt-BST interface; there are generally very sharp interfaces and no indications of amorphous interlayers. Nevertheless, some interfacial defects are indicated and a change of the lattice distance of the first layer has been observed at higher magnification,[27] however, a detailed interpretation seems speculative at present.

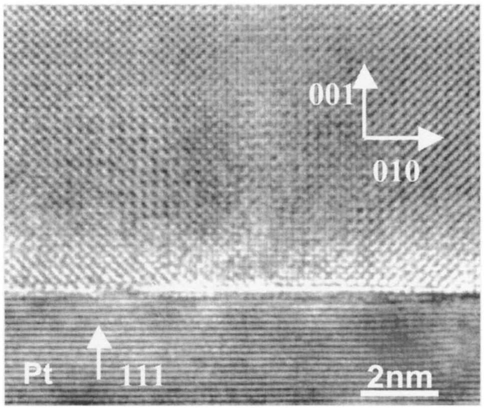

FIG. 12. Cross-sectional HRTEM of the Pt-(111)-BST interface.

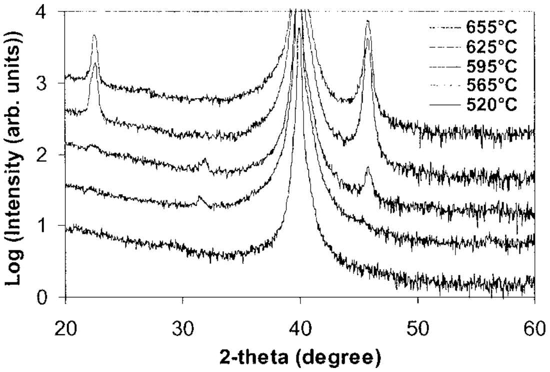

FIG. 13. XRD pattern for 30 nm films deposited at different temperatures.

B. Dependence on the deposition temperature

The general trends of the structural evolution are seen in the XRD patterns, Fig. 13. From an amorphous film at 520 °C there evolves a polycrystalline structure at 565 °C and finally the well-developed (100) texture for deposition temperatures above 600 °C. Additional details of the structure developed at 565 °C are revealed by HRTEM. Figures 14(a) and 14(b) show micrographs similar to Fig. 11, for a 30-nm thick film deposited at 565 °C. There is a random orientation of the grains, and the high magnification shows a high density of twins within the grains. Cross-sectional TEM images and SEM show in addition some interruptions in the grain growth and some deviations from the columnar structure.

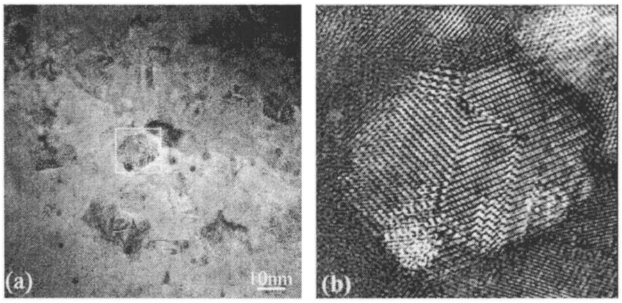

FIG. 14. HRTEM micrographs of backside-polished 30-nm BST films: $T_{\mathrm{dep}}=565$ °C; different magnifications are shown similar to Fig. 11.

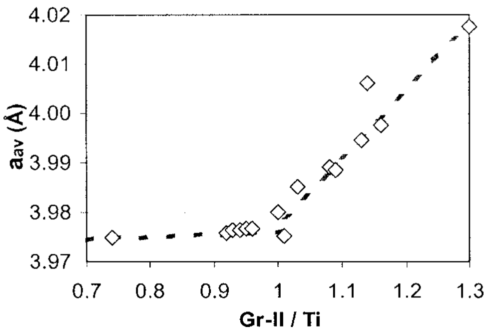

FIG. 15. Change of the average (strain corrected) lattice parameter of ~30-nm-thick BST films as a function of the stoichiometry ratio group-II/Ti.

C. Stoichiometry 1: Dependence on the group-II/Ti ratio

Figure 15 summarizes the lattice parameters for (100)-textured films grown at 655 °C; there is no change observed for the Ti-rich samples and a steady increase of the lattice parameter with a rising group-II content for the group-II-rich samples. Similar observations had been reported for MOCVD-deposited $SrTiO_3$ films[4] and for sputter-deposited BST (Ref. 28) and attributed to the incorporation of the excess group-II elements in the form of Ruddlesden-Popper phases. In addition, we observe a change of the peak profile, most clearly visible at the (400) reflection, $2\vartheta \sim 102°$, along with the variation of the average lattice parameter: there is a broadening and a tail to the low angle side, which indicates an inhomogeneous incorporation of the excess group-II elements (Fig. 16). Remarkably, these structures seem not very stable as there is a rearrangement to a more homogeneous structure during annealing in oxygen at a temperature of 550 °C. (This annealing was performed routinely as a post electrode deposition annealing step for all electrical measurements discussed below.) For the Ti-rich films there is no indication of a change of the lattice parameter. Such a behavior is compatible with the formation of precipitates of TiO_x at the grain boundaries, which is observed for high-temperature-sintered ceramics, and there has been an intensive search for the location of the surplus Ti in thin films. For very high Ti contents analytical TEM reveals stable precipitates of amorphous TiO_x,[29,30] however, for lower Ti content, group-II/Ti ~ 0.96, precipitates are found[30] or not.[29] In addition, there are indications from SFM investigations at single-crystalline $SrTiO_3$ for a incorporation of surplus Ti in the form of additional TiO_2 layers, which resemble the formation of Magneli phases.[31] This means that these layers do not imply a change of the lattice parameter, and are much more difficult to image than the SrO planes.

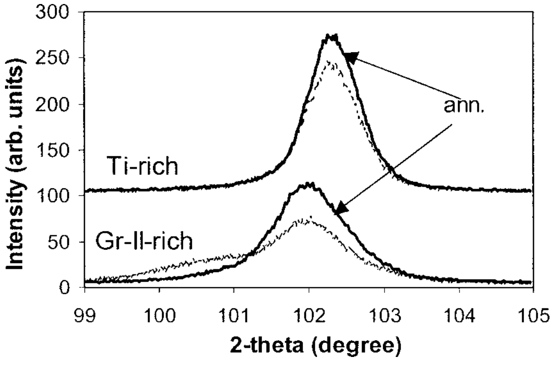

FIG. 16. Line shape of the (400) reflection for Ti-rich (group-II/Ti=0.93) and Gr-II-rich (group-II/Ti=1.03) films (T_{growth}=625 °C) and change after annealing at 550 °C.

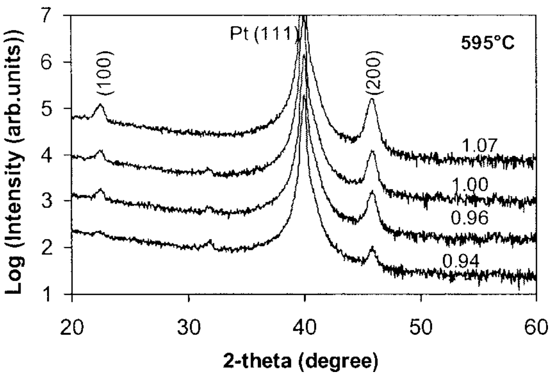

FIG. 17. Stoichiometry dependence of the texture of ~30-nm thick films, which were deposited at 595 °C

Generally, high T_{growth} results in the formation of perfectly columnar grains, regardless of the total film stoichiometry. Nevertheless, there is an influence on the grain growth at temperatures close to the transition to the polycrystalline growth. This is demonstrated by the XRD patterns in Fig. 17, which show at 595 °C a perfect (100) texture for group-II rich films but a more random grain orientation for the Ti-rich films, as already shown above in Fig. 13. The stoichiometry has also a significant impact on the surface morphology and grain size. The group-II-rich films show columnar grains of similar size, which seem to be peaked or faceted at the surface. This grain structure is reflected by the surface roughness observed by SFM, Fig. 18. Ti excess yields the formation of smaller and less well-resolved grains with a locally flat surface; however, the formation of larger bumps is observed again by SFM. Similar differences of the grain size have also been observed for sputter-deposited films.[28] The differences in the surface morphology may indicate different growth modes, e.g., growth on the inclined (111) or (110) facets for group-II-rich films and close to (100) for Ti-rich films. A more serious problem are the irregular bumps observed for Ti-rich films, which yield a rms roughness, which is similar to that of the group-II-rich films, although the films are locally more flat. This locally disturbed growth may be related to the incorporation of the Ti excess in the grain boundaries and perhaps to the so-called irregular grain growth observed for Ti-rich $BaTiO_3$ ceramics.[32–34]

D. Stoichiometry 2: Dependence on the Ba/Sr ratio, BST vs STO

In addition we examined the influence of the (Ba/Sr) ratio, which is otherwise fixed around (Ba/Sr=70/30). Figure 19 shows five films, which were grown at 655 °C with thickness between 23–32 nm. The composition was slightly group-II rich (group-II/Ti=1.01–1.05) and the (Ba/Sr) ratio was varied from 70/30 to 0/100 (pure STO) as indicated in

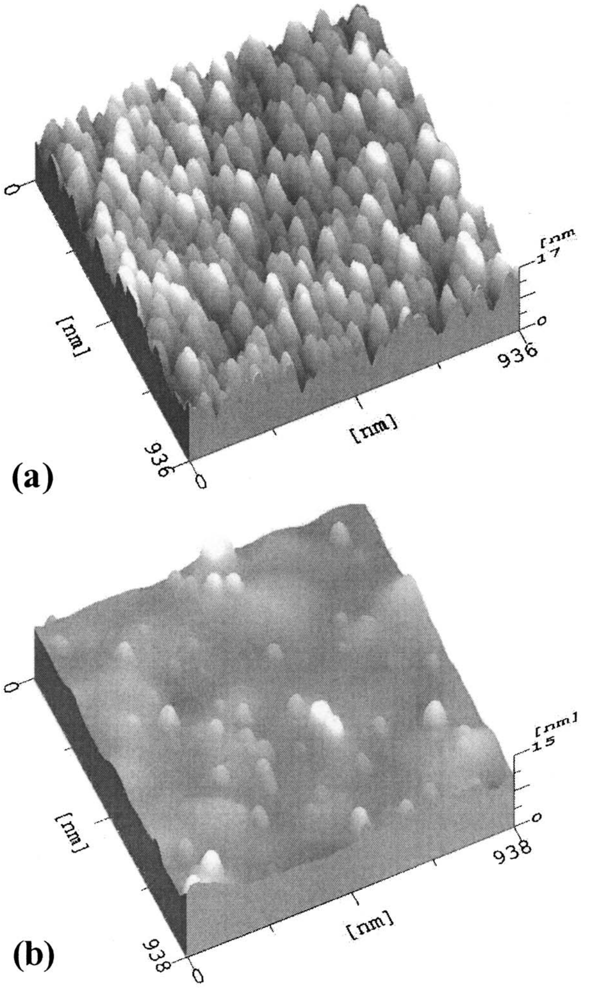

FIG. 18. Dependence of the surface morphology on the group-II/Ti ratio for films of ~30 nm thickness. (a) Group-II/Ti=1.07; the rms roughness is 2.46 nm; (b) group-II/Ti=0.95; the rms roughness is 3.26 nm.

the figure. We observe the expected clear shift of the (h00) peaks, and the decrease of the height of the (100) superstructure reflection as compared to the (200) fundamental reflection with lower Ba content. The measured lattice parameters of the *c* axis are summarized in Fig. 20 as a function of the composition *x*. After correction for the stress the cubic average lattice parameters follow the expected Vegard's law line for bulk data exactly (STO: $a=3.905$ Å, $(Ba_{0.7}Sr_{0.3})TiO_3:a=3.9778$ Å, and $BaTiO_3:(a^2c)^{1/3}=4.009\,95$ Å).

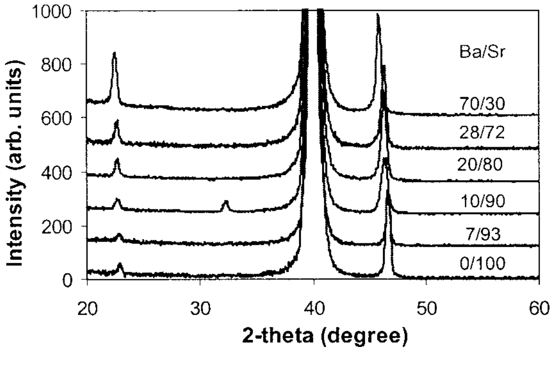

FIG. 19. XRD patterns for films of ~30 nm thickness and varying Ba content.

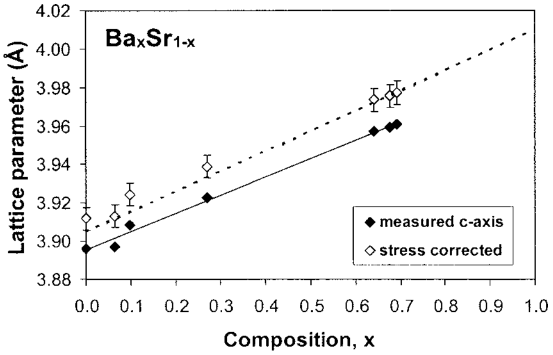

FIG. 20. Change of the lattice parameter of $Ba_xSr_{(1-x)}TiO3$ films as a function of the composition *x*. The *c*-axis parameter was measured at (002) and (004) reflections, closed symbols. The corresponding stress-corrected average cubic lattice parameter is given as open symbols. The dotted line represents Vegard's law for bulk samples.

For low Ba content there is some indication of the (110) reflection, which shows larger variations for different films. These deviations from the perfect (100) texture are supported by TEM, which additionally indicates larger fluctuations in the in-plane grain size. These observations indicate a less stable columnar growth for the STO. There is, however, no transition to a (111) texture, which might be expected due to the perfect lattice match in the stoichiometry region of Ba/Sr ~ 0.2, where a transition from tensile to compressive stress could be expected. Remarkably, such an epitaxial growth has been observed for CSD grown $SrTiO_3$ films.[13] This behavior indicates clearly that the lattice strain is not the dominant factor for the formation of the texture. As this dominant (100) texture seems not to be formed with other deposition techniques[11–13] we attribute this to a specially low (100) surface energy within the MOCVD environment.

E. Thickness dependence of grain structure and surface morphology

The observed thickness independence of the film structure is important for a straightforward evaluation of the electrical data in terms of thickness series. Generally, good co-

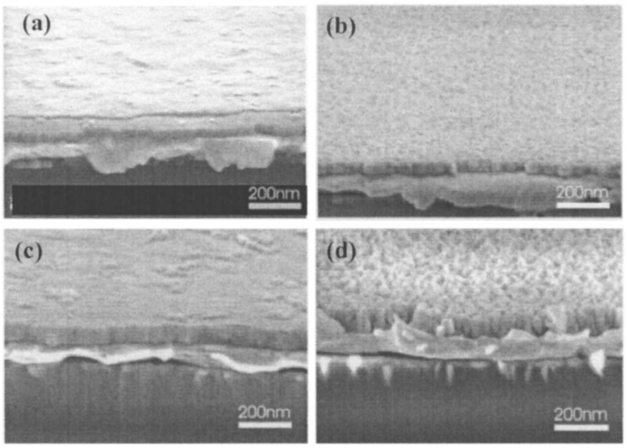

FIG. 21. Comparison of cross-sectional SEM micrographs from fracture surfaces of BST films grown at 655 °C on Pt electrodes. (a) 31-nm Ti-rich film [same as Fig. 18(b)]; (b) 33-nm group-II-rich film [same as Fig. 18(a)]; (c) 55-nm Ti-rich film; (d) 91-nm group-II-rich film.

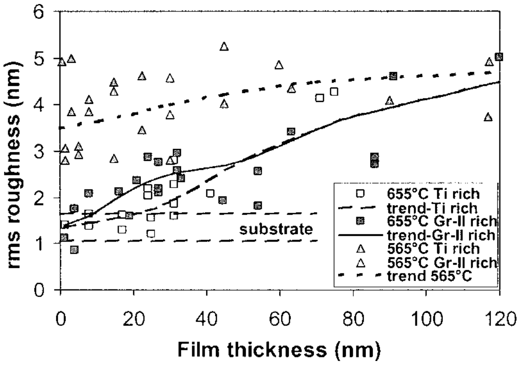

FIG. 22. Thickness dependence of the rms roughness of films deposited at 655 and 565 °C. For the films deposited at 655 °C there is a dependence on stoichiometry indicated for small thickness. The variation of the roughness of the Pt electrode is given by the dotted lines.

lumnar grain growth is observed by SEM (Ref. 25) and TEM (Ref. 26) for BST films after high temperature, $T \geqslant 595$ °C, depositions. The grain size depends to some extend on stoichiometry and only small changes with thickness are observed, Fig. 21.

The surface roughness determined over 1000×1000 nm^2 scanning areas is plotted in Fig. 22 as a function of the film thickness. For the randomly oriented films deposited at 565 °C we observe an average rms of 3–4 nm from the beginning and a very small further roughening up to values of 4–5 nm at 120 nm thickness. For the high-temperature-deposited films, the rms thickness variation is much determined by the Pt substrate for low thickness, up to ~20 nm; later on some roughening is observed along with further growth. In spite of the scatter of the data there is indication for a higher roughness for the group-II-rich films especially in the region from 10 to 30 nm; this difference reflects the different structure discussed above (Figs. 18 and 21). In qualitative agreement with earlier reports[9] the roughness increases for thicker films. Nevertheless, the roughening is limited to an extent that the relative roughness, rms/d, is decreasing with increasing thickness.

V. STRUCTURE-ELECTRICAL PROPERTY RELATIONS

It is generally observed that the permittivity of high-K thin-film capacitors shows some thickness dependence, which can be described phenomenologically by an interfacial layer, which yields a series capacity. This model assumes a bulk region of thickness t and relative permittivity ϵ_B and the two interface regions with thickness t_i which yield two capacitors of a lower relative permittivity ϵ_i. Considering the two electrodes as identical the resulting reciprocal capacitance of the film is given by Eq. (2) and the slope of a plot of $1/C$ vs thickness yields the bulk permittivity, and the intercept represents the interface capacitance.

$$\frac{A}{C} = \frac{2 \cdot A}{C_i} + \frac{A}{C_B} \approx \frac{2 \cdot t_i}{\varepsilon_0 \cdot \varepsilon_i} + \frac{t}{\varepsilon_0 \cdot \varepsilon_B}. \qquad (2)$$

The results for $(Ba_{0.7}Sr_{0.3})TiO_3$ films and STO films are summarized in Table II as obtained for a typical thickness range from 15 to 100 nm. For smaller thickness ranges the uncertainty in the slope and in the extrapolation values increases. As discussed previously[26] we observe an increase of the interface capacitance and of the bulk permittivity ε_B along with the improved microstructure after increasing T_{dep} from 565 to 655 °C. The low bulk permittivity for the low deposition temperature of 565 °C might be related to the changes in texture and perhaps even more important to the imperfection of the grains, which contain a large number of planer defects. There is no significant difference for different stoichiometries at 565 °C, although carbonates start to be formed for the group-II-rich films preferentially as evidenced by infrared absorption spectroscopy.[35] For $(Ba_{0.7}Sr_{0.3})TiO_3$ films deposited between 595 and 655 °C there is no significant difference observed. As the texture changes for these films, Figs. 13 and 17, this observation indicates that the perfection of the (100) texture has no major influence. This observation is consistent with the results for sputter-deposited films,[11,36] which show similarly good permittivity although there is no (100) texture, as discussed above. For these high-temperature-deposited films we observe, however, a clear indication of a stoichiometry dependency (group-II/Ti ratio), a decrease of the interfacial capacitance and an increase of the bulk permittivity with increasing Ti content of the films.[19] This different behavior of bulk permittivity and interfacial layers implies a complex behavior of the measured effective permittivity ϵ_{eff} of the films: for thick films where the bulk permittivity dominates the effective permittivity reaches a maximum for stoichiometric films as discussed in Ref. 2 for the case of ~60-nm thick films; for thin films of 20–30 nm, which are most relevant for DRAM applications, the interface becomes more important and we observe a slight increase of the effective permittivity for group-II/Ti > 1. The values of ε_i/t_i for the STO films are always at the upper limit of the values obtained for $(Ba_{0.7}Sr_{0.3})TiO_3$

TABLE II. Permittivity for $(Ba_{0.7}Sr_{0.3})TiO_3$ and $SrTiO_3$ films.

Film	T_{dep}(°C)	Group-II/Ti	ε_b[a]	$\varepsilon_i/2t_i$ (nm^{-1})	ε_{eff} for 20 nm	ε_{eff} for 60 nm
BST	565	0.94–1.06	250±60	5.4±1	74	142
	595	0.93–0.97	790±60	6.6±1	114	265
		0.98–1.02	800±60	7.1±1	120	277
		1.03–1.11	400±150	11.3±2	145	253
	655	0.91–0.95	750±30	7.1±2	120	278
		0.97–1.03	827±50	8.4±4	140	313
		1.03–1.10	500±50	11.2±3	155	284
STO	655	0.94–1.05	210±20	17±3	128	173

[a] Larger errors arise for limited thickness range of the available data.

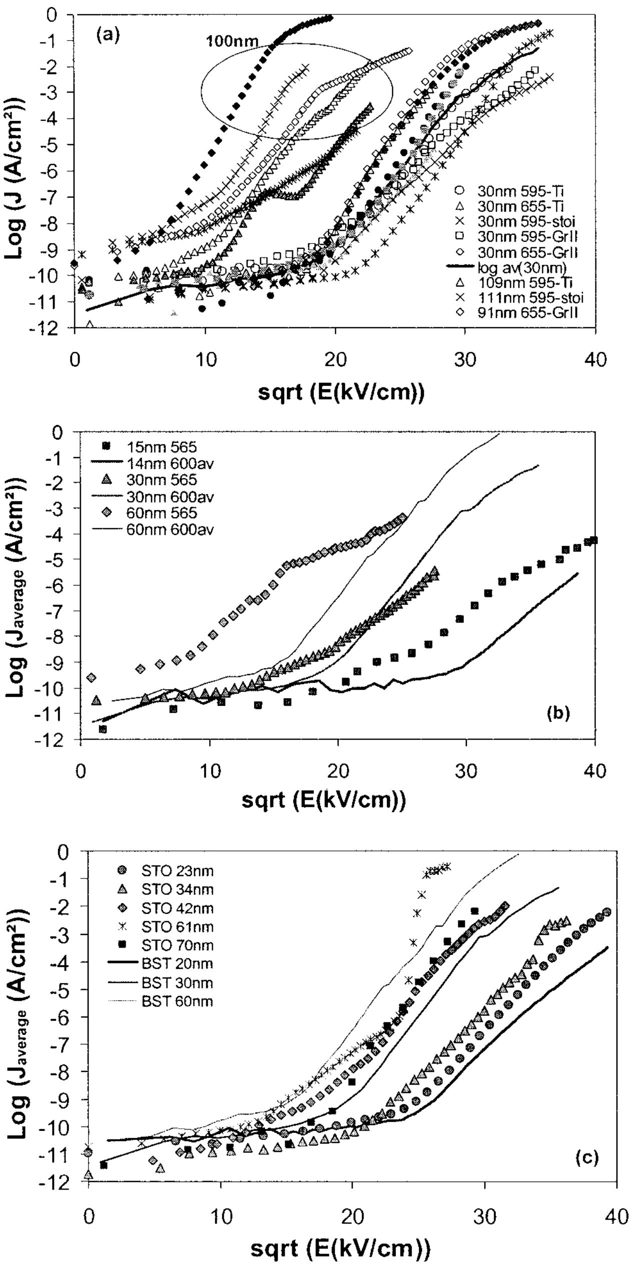

FIG. 23. Schottky plots of the leakage current for BST and STO films of different thicknesses. (a) Ti-rich and group-II-rich BST films of ~30 and ~100 nm thicknesses as-deposited at 595 and 655 °C. Positive and negative bias voltages are characterized by open and closed symbols, respectively. (b) Comparison of films deposited at 565 °C to the average values for films deposited at ⩾600 °C. (c) Comparison of STO and BST films deposited at $T \geqslant 600$ °C.

and no significant changes can be observed. Due to the better interface capacity the STO films reach the effective capacity of BST for the thinnest films.

The leakage currents are summarized in Fig. 23 in the form of Schottky plots. The field dependence of the leakage currents is seriously affected by the film thickness[19,35] and this unusual behavior corroborates the comparability of different published data as only films of similar thickness can be compared. At low fields we observe a rather slow increase of the currents, which might be partly due to the limited experimental resolution of $\sim 10^{-11}$ A/cm^2. At medium fields we observe for all films a steep slope, which yields the well-known unphysically low values for the optical dielectric constant ($\varepsilon_{\mathrm{optical}} < 1$). This deviation from a Schottky behavior can be understood within the dead layer model. The important point is the inhomogeneous distribution of the electric field: a large drop within the low-ϵ interfacial layer and a smaller one within the high-ϵ film.[37–39] Within this model the thickness dependence can be understood, too.[39] Figure 23(a) shows the variation of the leakage currents for ~30-nm thick films deposited at 595 and 655 °C with different group-II/Ti ratios. Measurements with negative and positive biases are shown as obtained for virgin pads in order to avoid degradation and/or polarization effects. Due to the scatter of the data no conclusion on a possible influence of the polarity seems reasonable at present. As in this logarithmic presentation the arithmetic average for all curves is close to the highest values the average of the logarithms is included as a reference. Within the variations, which are typically one order of magnitude,[38] there is no significant difference for the different deposition temperatures, and for the different group-II/Ti ratio. For the thickest films of ~100 nm there are even larger variations. Nevertheless, some trend is observed for these thick films: the group-II-rich films deposited at 655 °C show the highest leakage. This leakage behavior might be directly related to the higher surface roughness of these films as shown in Figs. 18 and 23 (the larger hillocks of the Ti-rich films will not hurt, but the more deep valleys at the grain boundaries of the group-II rich films do). Hence, these results for the thicker films reproduce earlier conclusions,[2] which reported better leakage behavior for Ti-rich films based on data from ~60-nm thick films. However, this behavior is no longer observed for the technological more relevant thin films of 15–30 nm thickness.

Figure 23(b) compares films deposited at 565 °C to the high-temperature-deposited films. The 565 °C films have a higher leakage current at low fields and approach and even cross the lines for the 655 °C films at higher fields. This behavior might be related to the higher defect density of the 565 °C deposited films. This conclusion is consistent with the simulations,[38,39] which suggest that leakage currents at low fields are essentially bulk limited.

Figure 23(c) compares films of similar thickness of BST and STO. In spite of the uncertainties of the individual plots, we consistently observe a lower leakage for STO films. Again, a direct comparison to published data is corroborated by the dominating thickness dependence, e.g., a comparison of a 150-nm-thick STO film with a 50-nm BST film[40] cannot show the same trends. Nevertheless, a similar difference has been reported for sputter-deposited 60-nm thick films of $(\mathrm{Ba}_{0.5}\mathrm{Sr}_{0.5})\mathrm{TiO}_3$ and STO (Ref. 41) at a bias voltage of 3.3 V; in addition the breakdown voltages for STO films were lower than for the BST films.

VI. SUMMARY AND CONCLUSION

We investigated the deposition of the mixed oxide, BST, from the earliest growth stages. We observed a rather homogeneous nucleation on the Pt grains at 565 °C and a more heterogeneous nucleation at grain boundaries at 655 °C. This difference is easily rationalized by the faster diffusion at the higher temperature. Hence, the grain boundaries seem to be the energetically favored nucleation sites and, starting from different points at the grain boundary of the Pt, the films grow with different in-plane orientations such that the grain size of the films always remains smaller than that of the underlying Pt.

The films deposited at 565 and 655 °C differ in texture and in the perfection of the grains. In addition differences in microstructure and surface morphology are observed along with the variation of the stoichiometry, Ba/Sr as well as group-II/Ti. The columnar growth is rather stable up to thickness of ~100 nm; only for STO grain disruptions are observed more frequently. The strong (100) texture of the BST, which is different to observations for other deposition methods, is attributed to the special chemical environment at the surface.

These microstructural and chemical differences are shown to affect the most relevant electrical properties, permittivity, and leakage current. Remarkably the interfacial properties of STO are less sensitive to stoichiometry variations than $(Ba_{0.7}Sr_{0.3})TiO_3$ and their value is at the upper limit obtained for $(Ba_{0.7}Sr_{0.3})TiO_3$. Leakage currents show complex field dependence and are dominated by the strong thickness dependence. Nevertheless, some trends can be deduced: STO has slightly improved leakage behavior as compared to $(Ba_{0.7}Sr_{0.3})TiO_3$, the improved crystallinity obtained at deposition temperatures $\geqslant 600$ °C is favorable especially for low fields, and surface roughness is important especially at larger film thickness.

ACKNOWLEDGMENTS

We want to thank W. Krumpen for his support by the XRF analysis of the films and Dr. A. Besmehn for part of the XPS analysis. We gratefully acknowledge the support by AIXTRON AG, Aachen.

[1] A. I. Kingon, J. P. Maria, and S. K. Streiffer, Nature (London) **406**, 1032 (2000).

[2] S. R. Summerfelt, in *Thin Film Ferroelectric Materials and Devices*, edited by R. Ramesh (Kluwer, Boston, 1999), p.1–42.

[3] C. S. Hwang, Mater. Sci. Eng., B **B56**, 178 (1999).

[4] M. Yoshida, H. Yabuta, S. Yamamichi, H. Yamaguchi, S. Sone, K. Iizuka, S. Nishimoto, and Y. Kato, J. Electroceram. **3**, 123 (1999).

[5] T. Horikawa *et al.*, Mater. Res. Soc. Symp. Proc. **541**, 3 (1999).

[6] M. Tarutani, M. Yamamuka, T. Takenaga, T. Kuriowa, and T. Horikawa, Thin Solid Films **409**, 8 (2002).

[7] A. I. Kingon and S. K. Streiffer, Curr. Opin. Solid State Mater. Sci. **4**, 39 (1999).

[8] H. Shen *et al.*, Mater. Res. Soc. Symp. Proc. **493**, 33 (1998).

[9] S. M. Bilodeau *et al.*, J. Korean Phys. Soc. **32**, S1591 (1998).

[10] P. Ehrhart *et al.*, Mater. Res. Soc. Symp. Proc. **655**, CC9.4.1 (2001).

[11] J. D. Baniecki, T. Shioga, and K. Kurihara, Integr. Ferroelectr. **46**, 221 (2002).

[12] X. H. Zhu, H. L. W. Chan, C. L. Choi, and K. W. Wong, Integr. Ferroelectr. **45**, 131 (2002).

[13] C. L. Jia, K. Urban, S. Hoffmann, and R. Waser, J. Mater. Res. **13**, 2206 (1998).

[14] K. Tokita, M. Aratani, and H. Funakubo, Appl. Phys. Lett. **81**, 898 (2002).

[15] P. Ehrhart *et al.*, Integr. Ferroelectr. **30**, 183 (2000).

[16] S. Regnery *et al.*, J. Eur. Ceram. Soc. **24**, 271 (2004).

[17] U. Breuer, W. Krumpen, and F. Fitsilis, Anal. Bioanal. Chem. **375**, 906 (2003).

[18] C. Schmidt, W. Lehnert, T. Leistner, L. Frey, and H. Ryssel, J. Phys. IV **9**, Pr8-575 (1999).

[19] S. Regnery *et al.*, Mater. Res. Soc. Symp. Proc. **748**, U15.6.1 (2003).

[20] S. K. Streiffer, C. Basceri, C. B. Parker, S. E. Lash, and A. I. Kingon, J. Appl. Phys. **86**, 4565 (1999).

[21] A. Segmüller and M. Murakami, in *Treatise on Materials Science and Technology: Analytical Techniques for Thin Films*, edited by K. N. Tu and R. Rosenberg (Academic, New York, 1988) pp.143–200.

[22] T. M. Shaw, Z. Suo, M. Huang, E. Liniger, R. B. Laibowitz, and J. D. Baniecki, Appl. Phys. Lett. **75**, 2129 (1999).

[23] G. Simmons and H. Wang, *Single Crystal Elastic Constants and Calculated Aggregate Properties: A Handbook* (The M.I.T. Press, Cambridge, MA, 1971).

[24] S. K. Streiffer, C. Basceri, C. B. Parker, S. E. Lash, J. Christman, H. Maiva, and A. I. Kingon, *Proceedings ISAF-1998*, IEEE Report No. 98CH36245, 1998, p. 31.

[25] W. Y. Park and C. S. Hwang, Appl. Phys. Lett. **85**, 5313 (2004).

[26] P. Ehrhart, F. Fitsilis, S. Regnery, R. Waser, F. Schienle, M. Schumacher, H. Juergensen, and W. Krumpen, Integr. Ferroelectr. **45**, 59 (2002).

[27] H. Z. Jin, J. Zhu, P. Ehrhart, F. Fitsilis, C. L. Jia, S. Regnery, K. Urban, and R. Waser, Thin Solid Films **429**, 282 (2003).

[28] S. Yamamichi, H. Yabuta, T. Sakuma, and Y. Miyasaka, Appl. Phys. Lett. **64**, 1644 (1994).

[29] S. Stemmer, S. K. Streiffer, N. D. Browning, and A. I. Kingon, Appl. Phys. Lett. **74**, 2432 (1999).

[30] I. Levin, R. D. Leapman, D. L. Kaiser, P. C. Van Buskirk, S. Bilodeau, and R. Carl, Appl. Phys. Lett. **75**, 1299 (1999).

[31] K. Szot and W. Speier, Phys. Rev. B **60**, 5909 (1999).

[32] T. Yamamoto, Y. Ikuhara, K. Hayashi, and T. Sakuma, J. Mater. Res. **13**, 3449 (1998).

[33] B.-K. Lee, S.-Y. Chung, and S.-J. Kang, Acta Mater. **48**, 1575 (2001).

[34] B.-K. Lee and S.-J. Kang, Acta Mater. **49**, 1373 (2001)

[35] F. Fitsilis, S. Regnery, P. Ehrhart, R. Waser, F. Schienle, M. Schumacher, and H. Juergensen, Integr. Ferroelectr. **38**, 211 (2001).

[36] B. T. Lee and C. S. Hwang, Appl. Phys. Lett. **77**, 124 (2000).

[37] G. Steinlesberger, H. Reisinger, H. Bachhofer, H. Schroeder, and W. S. M. Werner, Integr. Ferroelectr. **38**, 249 (2001).

[38] H. Schroeder and S. Schmitz, Mater. Res. Soc. Symp. Proc. **748**, U6.2.1 (2003).

[39] H. Schroeder and S. Schmitz, Appl. Phys. Lett. **83**, 4381 (2003).

[40] G. W. Dietz, M. Schumacher, R. Waser, S. K. Streiffer, C. Basceri, and A. J. Kingon, J. Appl. Phys. **82** 2359 (1997).

[41] B. A. Baumert *et al.*, Integr. Ferroelectr. **17**, 165 (1977).